Atmospheric correction using near-infrared bands for satellite ocean color data processing in the turbid western Pacific region

Menghua Wang,[1,*] Wei Shi,[1,2] and Lide Jiang[1,2]

[1]*NOAA National Environmental Satellite, Data, and Information Service, Center for Satellite Applications and Research, E/RA3, Room 102, 5200 Auth Road, Camp Springs, Maryland 20746, USA*
[2]*CIRA at Colorado State University, Fort Collins, Colorado, USA*
[*]*Menghua.Wang@noaa.gov*

Abstract: A regional near-infrared (NIR) ocean normalized water-leaving radiance ($nL_w(\lambda)$) model is proposed for atmospheric correction for ocean color data processing in the western Pacific region, including the Bohai Sea, Yellow Sea, and East China Sea. Our motivation for this work is to derive ocean color products in the highly turbid western Pacific region using the Geostationary Ocean Color Imager (GOCI) onboard South Korean Communication, Ocean, and Meteorological Satellite (COMS). GOCI has eight spectral bands from 412 to 865 nm but does not have shortwave infrared (SWIR) bands that are needed for satellite ocean color remote sensing in the turbid ocean region. Based on a regional empirical relationship between the NIR $nL_w(\lambda)$ and diffuse attenuation coefficient at 490 nm ($K_d(490)$), which is derived from the long-term measurements with the Moderate-resolution Imaging Spectroradiometer (MODIS) on the Aqua satellite, an iterative scheme with the NIR-based atmospheric correction algorithm has been developed. Results from MODIS-Aqua measurements show that ocean color products in the region derived from the new proposed NIR-corrected atmospheric correction algorithm match well with those from the SWIR atmospheric correction algorithm. Thus, the proposed new atmospheric correction method provides an alternative for ocean color data processing for GOCI (and other ocean color satellite sensors without SWIR bands) in the turbid ocean regions of the Bohai Sea, Yellow Sea, and East China Sea, although the SWIR-based atmospheric correction approach is still much preferred. The proposed atmospheric correction methodology can also be applied to other turbid coastal regions.

©2012 Optical Society of America

OCIS codes: (010.0010) Atmospheric and oceanic optics; (010.1285) Atmospheric correction; (010.4450) Oceanic optics; (010.1290) Atmospheric optics.

References and links

1. H. R. Gordon and M. Wang, "Retrieval of water-leaving radiance and aerosol optical thickness over the oceans with SeaWiFS: a preliminary algorithm," Appl. Opt. **33**(3), 443–452 (1994).
2. IOCCG, "Atmospheric Correction for Remotely-Sensed Ocean-Colour Products," M. Wang (Ed.), *Reports of International Ocean-Colour Coordinating Group*, No. 10, IOCCG, Dartmouth, Canada (2010).
3. J. E. O'Reilly, S. Maritorena, B. G. Mitchell, D. A. Siegel, K. L. Carder, S. A. Garver, M. Kahru, and C. R. McClain, "Ocean color chlorophyll algorithms for SeaWiFS," J. Geophys. Res. **103**(C11), 24937–24953 (1998).
4. J. L. Mueller, "SeaWiFS algorithm for the diffuse attenuation coefficient, K(490), using water-leaving radiances at 490 and 555 nm," SeaWiFS Postlaunch Tech. Rep. Ser., vol. 11, NASA Tech. Memo. 2000–206892, S. B. Hooker and E. R. Firestone, eds., NASA Goddard Space Flight Center, Greenbelt, Maryland, pp. 24–27 (2000).
5. A. Morel, Y. Huot, B. Gentili, P. J. Werdell, S. B. Hooker, and B. A. Franz, "Examining the consistency of products derived from various ocean color sensors in open ocean (Case 1) waters in the perspective of a multi-sensor approach," Remote Sens. Environ. **111**(1), 69–88 (2007).
6. M. Wang, S. Son, and J. L. W. Harding, Jr., "Retrieval of diffuse attenuation coefficient in the Chesapeake Bay and turbid ocean regions for satellite ocean color applications," J. Geophys. Res. **114**(C10), C10011 (2009), doi:10.1029/2009JC005286.

7. H. R. Gordon, J. W. Brown, and R. H. Evans, "Exact Rayleigh scattering calculations for use with the Nimbus-7 Coastal Zone Color Scanner," Appl. Opt. **27**(5), 862–871 (1988).
8. H. R. Gordon and M. Wang, "Surface-roughness considerations for atmospheric correction of ocean color sensors. I: The Rayleigh-scattering component," Appl. Opt. **31**(21), 4247–4260 (1992).
9. M. Wang, "The Rayleigh lookup tables for the SeaWiFS data processing: Accounting for the effects of ocean surface roughness," Int. J. Remote Sens. **23**(13), 2693–2702 (2002).
10. M. Wang, "A refinement for the Rayleigh radiance computation with variation of the atmospheric pressure," Int. J. Remote Sens. **26**(24), 5651–5663 (2005).
11. M. Wang, "A sensitivity study of SeaWiFS atmospheric correction algorithm: Effects of spectral band variations," Remote Sens. Environ. **67**(3), 348–359 (1999).
12. M. Wang, "Aerosol polarization effects on atmospheric correction and aerosol retrievals in ocean color remote sensing," Appl. Opt. **45**(35), 8951–8963 (2006).
13. A. Morel and D. Antoine, "Heating rate within the upper ocean in relation to its bio-optical state," J. Phys. Oceanogr. **24**(7), 1652–1665 (1994).
14. Y. Wu, C. Tang, S. Sathyendranath, and T. Platt, "The impact of bio-optical heating on the properties of the upper ocean: A sensitivity study using a 3-D circulation model for the Labrador Sea," Deep Sea Res. Part II Top. Stud. Oceanogr. **54**(23-26), 2630–2642 (2007).
15. S. Sathyendranath, T. Platt, C. M. Caverhill, R. Warnock, and M. Lewis, "Remote sensing of oceanic primary production: Computations using a spectral model," Deep-Sea Res. **36**(3), 431–453 (1989).
16. Z. P. Lee, K. L. Carder, and R. A. Arnone, "Deriving inherent optical properties from water color: a multiband quasi-analytical algorithm for optically deep waters," Appl. Opt. **41**(27), 5755–5772 (2002).
17. H. R. Gordon, "Atmospheric correction of ocean color imagery in the Earth Observing System era," J. Geophys. Res. **102**(D14), 17081–17106 (1997).
18. S. W. Bailey and P. J. Werdell, "A multi-sensor approach for the on-orbit validation of ocean color satellite data products," Remote Sens. Environ. **102**(1-2), 12–23 (2006).
19. C. R. McClain, "A decade of satellite ocean color observations," Annu. Rev. Mar. Sci. **1**(1), 19–42 (2009).
20. M. Wang and W. Shi, "Estimation of ocean contribution at the MODIS near-infrared wavelengths along the east coast of the U.S.: Two case studies," Geophys. Res. Lett. **32**(13), L13606 (2005), doi:10.1029/2005GL022917.
21. S. J. Lavender, M. H. Pinkerton, G. F. Moore, J. Aiken, and D. Blondeau-Patissier, "Modification to the atmospheric correction of SeaWiFS ocean color images over turbid waters," Cont. Shelf Res. **25**(4), 539–555 (2005).
22. D. A. Siegel, M. Wang, S. Maritorena, and W. Robinson, "Atmospheric correction of satellite ocean color imagery: the black pixel assumption," Appl. Opt. **39**(21), 3582–3591 (2000).
23. K. G. Ruddick, F. Ovidio, and M. Rijkeboer, "Atmospheric correction of SeaWiFS imagery for turbid coastal and inland waters," Appl. Opt. **39**(6), 897–912 (2000).
24. R. P. Stumpf, R. A. Arnone, R. W. Gould, P. M. Martinolich, and V. Ransibrahmanakul, "A partially coupled ocean-atmosphere model for retrieval of water-leaving radiance from SeaWiFS in coastal waters," SeaWiFS Postlaunch Tech. Rep. Ser., vol. 22, NASA Tech. Memo. 2003–206892, S. B. Hooker and E. R. Firestone, eds., NASA Goddard Space Flight Center, Greenbelt, Maryland, pp. 51–59 (2003).
25. S. W. Bailey, B. A. Franz, and P. J. Werdell, "Estimation of near-infrared water-leaving reflectance for satellite ocean color data processing," Opt. Express **18**(7), 7521–7527 (2010).
26. M. Wang, "Remote sensing of the ocean contributions from ultraviolet to near-infrared using the shortwave infrared bands: simulations," Appl. Opt. **46**(9), 1535–1547 (2007).
27. M. Wang and W. Shi, "The NIR-SWIR combined atmospheric correction approach for MODIS ocean color data processing," Opt. Express **15**(24), 15722–15733 (2007).
28. M. Wang, S. Son, and W. Shi, "Evaluation of MODIS SWIR and NIR-SWIR atmospheric correction algorithm using SeaBASS data," Remote Sens. Environ. **113**(3), 635–644 (2009).
29. M. Wang, J. Tang, and W. Shi, "MODIS-derived ocean color products along the China east coastal region," Geophys. Res. Lett. **34**(6), L06611 (2007), doi:10.1029/2006GL028599.
30. M. Wang, W. Shi, and J. Tang, "Water property monitoring and assessment for China's inland Lake Taihu from MODIS-Aqua measurements," Remote Sens. Environ. **115**(3), 841–854 (2011), doi:10.1016/j.rse.2010.11.012.
31. G. M. Hale and M. R. Querry, "Optical constants of water in the 200 nm to 200 μm wavelength region," Appl. Opt. **12**(3), 555–563 (1973).
32. W. Shi and M. Wang, "An assessment of the black ocean pixel assumption for MODIS SWIR bands," Remote Sens. Environ. **113**(8), 1587–1597 (2009).
33. W. Shi and M. Wang, "Characterization of global ocean turbidity from Moderate Resolution Imaging Spectroradiometer ocean color observations," J. Geophys. Res. **115**(C11), C11022 (2010), doi:10.1029/2010JC006160.
34. W. Shi and M. Wang, "Satellite observations of the seasonal sediment plume in central East China Sea," J. Mar. Syst. **82**(4), 280–285 (2010), doi:10.1016/j.jmarsys.2010.06.002.
35. M. Zhang, J. Tang, Q. Dong, Q. Song, and J. Ding, "Retrieval of total suspended matter concentration in the Yellow and East China Seas from MODIS imagery," Remote Sens. Environ. **114**(2), 392–403 (2010).
36. H. R. Gordon, O. B. Brown, R. H. Evans, J. W. Brown, R. C. Smith, K. S. Baker, and D. K. Clark, "A semianalytic radiance model of ocean color," J. Geophys. Res. **93**(D9), 10909–10924 (1988).
37. M. Wang, K. D. Knobelspiesse, and C. R. McClain, "Study of the Sea-Viewing Wide Field-of-View Sensor (SeaWiFS) aerosol optical property data over ocean in combination with the ocean color products," J. Geophys. Res. **110**(D10), D10S06 (2005), doi:10.1029/2004JD004950.

38. M. Wang and W. Shi, "Satellite observed algae blooms in China's Lake Taihu," Eos Trans. AGU **89**(22), 201–202 (2008), doi:10.1029/2008EO220001.
39. W. Shi, M. Wang, X. Li, and W. G. Pichel, "Ocean sand ridge signatures in the Bohai Sea observed by satellite ocean color and synthetic aperture radar measurements," Remote Sens. Environ. **115**(8), 1926–1934 (2011), doi:10.1016/j.rse.2011.03.015.
40. S. Son, M. Wang, and J. Shon, "Satellite observations of optical and biological properties in the Korean dump site of the Yellow Sea," Remote Sens. Environ. **115**(2), 562–572 (2011), doi:10.1016/j.rse.2010.10.002.
41. S. Son and M. Wang, "Environmental responses to a land reclamation project in South Korea," Eos Trans. AGU **90**(44), 398–399 (2009).
42. W. Shi, M. Wang, and L. Jiang, "Spring-neap tidal effects on satellite ocean color observations in the Bohai Sea, Yellow Sea, and East China Sea," J. Geophys. Res. **116**, C12932 (2011), doi:10.1029/2011JC007234.

1. Introduction

Satellite ocean color retrievals such as normalized water-leaving radiance spectra ($nL_w(\lambda)$) [1,2], chlorophyll-a concentration (Chl-a) [3], and water diffuse attenuation coefficient at the wavelength of 490 nm ($K_d(490)$) [4–6] are computed after removing atmospheric radiance contributions and ocean surface effects from the top-of-atmosphere (TOA) radiance $L_t(\lambda)$ measured by satellite ocean color sensors such as the Sea-viewing Wide Field-of-view Sensor (SeaWiFS), the Moderate-resolution Imaging Spectroradiometer (MODIS), and the Medium Resolution Imaging Spectrometer (MERIS). For the blue wavelengths, the atmosphere radiance contribution, which includes atmosphere molecules (Rayleigh) radiance $L_r(\lambda)$ [7–10], atmospheric aerosol radiance $L_A(\lambda)$ (including Rayleigh-aerosol interactions) [1, 11, 12], can account for up to ~90% of the TOA radiance measurements [2]. Thus, accurate estimation of the atmospheric contributions in the TOA radiance is crucial in order to compute the normalized water-leaving radiance spectra $nL_w(\lambda)$, and consequently derive ocean optical, biological, and biogeochemical properties for studying, understanding, and monitoring the global and regional ocean variability and changes.

Particularly, the satellite-derived water diffuse attenuation coefficient $K_d(490)$ can be related to light penetration and availability in aquatic system. The $K_d(490)$ is an important parameter to understand not only physical processes such as the heat transfer in the ocean upper layer [13, 14], but also biological processes such as phytoplankton photosynthesis in the ocean euphotic zone [15]. For global open oceans, $K_d(490)$ can be accurately derived from satellite ocean color sensors (e.g., SeaWiFS, MODIS) using empirical models either through the blue-green $nL_w(\lambda)$ ratio [4] or using the relationship of $K_d(490)$ and chlorophyll-a concentration [5]. Semi-analytical approaches based on radiative transfer models have also been used [16]. In effect, these models all use the blue-green $nL_w(\lambda)$ data for deriving satellite $K_d(490)$ product. To provide improved $K_d(490)$ data in coastal turbid waters, a $K_d(490)$ model using $nL_w(\lambda)$ at blue, green, and red bands has been proposed and shown significantly improved $K_d(490)$ results in turbid waters [6]. It has been shown that for turbid waters $K_d(490)$ has strong correlation to $nL_w(\lambda)$ at the red band [6]. In fact, for highly turbid waters, $K_d(490)$ can be well correlated to $nL_w(\lambda)$ at the near-infrared (NIR) bands.

For the current and future global ocean color satellite sensors such as SeaWiFS, MODIS, and Visible Infrared Imager Radiometer Suite (VIIRS), the atmospheric correction for producing the global ocean color products is based on the *Gordon and Wang* (1994) [1] algorithm. Specifically, the algorithm uses two NIR bands to determine the aerosol type and compute the atmospheric effects in the visible by extrapolating the aerosol effect from the NIR into visible bands using aerosol models [1, 11, 17]. One assumption for the *Gordon and Wang* (1994) [1] algorithm is that the NIR ocean contribution is negligible in order to determine the aerosol type. For global open ocean waters, both SeaWIFS and MODIS have been producing high-quality ocean color products [18, 19].
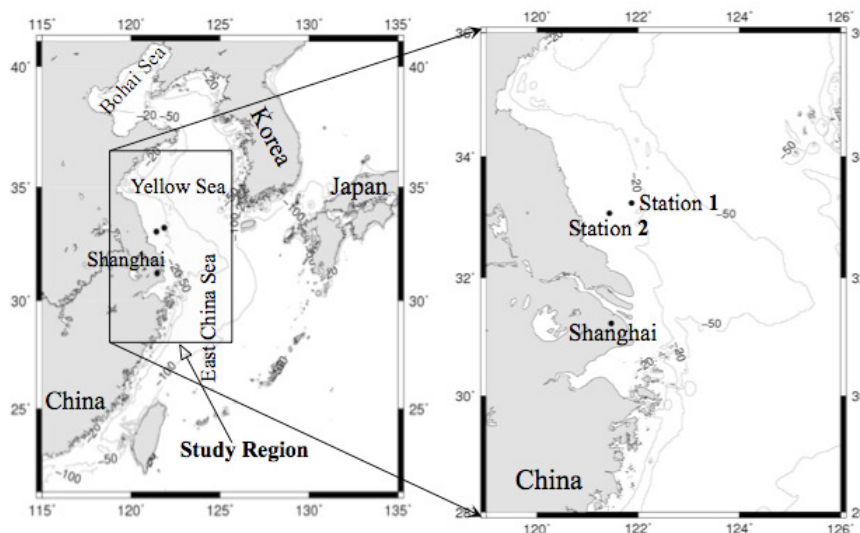
Fig. 1. Map of the western Pacific region, which includes the Bohai Sea, Yellow Sea, and East China Sea with isobaths of 20, 50, and 100 m. The highly turbid waters in this study are outlined in the box with marked pseudo-stations 1 (33.24°N, 121.87°E) and 2 (33.07°N, 121.43°E) for detailed data analyses.

In the coastal turbid regions and highly productive waters, the NIR ocean contributions are not negligible [20–24]. In order to remove the NIR ocean contributions in the turbid or productive waters so that the "black pixel assumption" in the NIR wavelengths can be valid for employing the *Gordon and Wang* (1994) [1] type atmospheric correction algorithm, various approaches are investigated. *Siegel et al.* (2000) [22] used the chlorophyll-a estimation to determine the NIR $nL_w(\lambda)$; *Lavender et al.* (2005) [21] used the sediment estimation to compute NIR $nL_w(\lambda)$; *Ruddick et al.* (2000) [23] fixed the aerosol and backscattering type and then solved for both the NIR $nL_w(\lambda)$ and NIR aerosol reflectance simultaneously; and *Stump et al.* (2003) [24] used a bio-optical model for absorptions in the red band, and then used that and $nL_w(\lambda)$ in the red band to compute NIR $nL_w(\lambda)$. In a more recent effort, *Bailey et al.* (2010) [25] further tuned and improved the *Stump et al.* (2003) [24] approach by applying optical modeling to compute the $nL_w(\lambda)$ from the absorption coefficient and $nL_w(\lambda)$ in the red band.

In recent years, an atmospheric correction algorithm using the shortwave infrared (SWIR) bands has been proposed [26, 27] and demonstrated to derive improved ocean (water) color products in turbid coastal ocean regions [28, 29] and inland lake waters [30]. Waters are more strongly absorbent at the SWIR bands (i.e., 1240, 1640, and 2130 nm for MODIS) than at the NIR wavelengths [31], i.e., water absorptions at the three MODIS SWIR bands are at least one order higher than those in the NIR bands. Significantly higher water absorptions at the SWIR bands indicate that for the highly turbid regions or productive waters, ocean can still be black for the SWIR bands even though there are significant $nL_w(\lambda)$ contributions in the NIR wavelengths [32]. Thus, water-leaving radiance in the visible and NIR wavelengths can be derived from the SWIR atmospheric correction algorithm for the highly turbid waters.

The western Pacific region (Fig. 1) covers some of the most turbid waters in the world, i.e., the Bohai Sea (BS), Yellow Sea (YS), and East China Sea (ECS) [33, 34]. Total suspended matter (TSM) concentration in the region can reach up to ~100 g m^{-3} [35]. Significant NIR ocean radiance contributions can be found along the coast of the Yellow Sea and the East China Sea [29, 33]. For example, the normalized water-leaving radiance at the NIR 748 nm ($nL_w(748)$) can reach over ~3 mW cm^{-2} μm^{-1} sr^{-1} in the Hangzhou Bay of China's east coastal region [29]. The complexity of the water property in these regions suggests that the NIR-modeling scheme such as that proposed by *Stump et al.* (2003) [24] or

Bailey et al. (2010) [25] cannot work properly; thus satellite ocean color remote sensing in the western Pacific is significantly limited in these highly turbid coastal zones. On the other hand, *Wang et al.* (2007; 2011) [29, 30] demonstrated that the SWIR-based atmospheric correction algorithm can be used to derive reasonably accurate $nL_w(\lambda)$ spectra data and other ocean color products in the Bohai Sea, Yellow Sea, and East China Sea, as well as in a turbid inland Lake Taihu. These studies indeed quantify and characterize the ocean optical features such as the $nL_w(\lambda)$ from deep blue (412 nm) to NIR (869 nm) wavelengths as well as the other optical, biological, and biogeochemical parameters such as $K_d(490)$ [6] and TSM concentration [35] in these turbid waters. Thus, the SWIR-based atmospheric correction algorithm provides opportunity to quantitatively estimate the NIR $nL_w(\lambda)$ in the region in order to carry out the NIR-based satellite ocean color data processing without the SWIR radiance measurements.

Our motivation for this work is to derive ocean color product data in the highly turbid western Pacific region using the Geostationary Ocean Color Imager (GOCI) onboard South Korean Communication, Ocean, and Meteorological Satellite (COMS), which was launched in June of 2010. GOCI has local area coverage of the western Pacific region (Fig. 1) and eight spectral bands covering from the blue to the NIR wavelengths (412–865 nm), but no SWIR bands. For such often highly turbid ocean regions, previously proposed NIR radiance models for atmospheric correction usually do not work properly. Thus, a new regional NIR radiance model needs to be developed. In this study, we use the long-term MODIS-Aqua-measured $nL_w(\lambda)$ in the NIR bands that have been derived using the SWIR-based atmospheric correction algorithm and water diffuse attenuation coefficient at 490 nm ($K_d(490)$) [6] to build an empirical relationship between the NIR $nL_w(\lambda)$ and $K_d(490)$. It is noted that $K_d(490)$ data are derived from MODIS-Aqua measurements using *Wang et al.* (2009) $K_d(490)$ algorithm [6] that provides improved $K_d(490)$ data in turbid coastal waters [6]. An iterative scheme with the NIR-based atmospheric correction algorithm has been developed in order to derive valid $nL_w(\lambda)$ in highly turbid coastal regions. Normalized water-leaving radiance spectra and other ocean color products derived from MODIS-Aqua using this new NIR-corrected atmospheric correction approach are further compared, evaluated, and validated quantitatively with the same ocean color parameters derived from the SWIR-based ocean color data processing.

2. Empirical relationship of the NIR $nL_w(748)$ and $nL_w(869)$ vs. $K_d(490)$

As discussed previously, in order to carry out the NIR-based atmospheric correction algorithm [1] for satellite ocean color data processing in coastal turbid waters, it is crucial that the NIR ocean radiance contributions be accurately accounted for [21–24]. Therefore, accurately and effectively estimating the NIR $nL_w(\lambda)$ contributions in coastal turbid water regions, e.g., the western Pacific region, for carrying out the NIR-based atmospheric correction (without using the SWIR bands) for satellite ocean color data processing is the main focus of this section.

In a recent study, *Shi and Wang* (2009) [32] show that $nL_w(\lambda)$ in the red band ($nL_w(645)$) and the NIR band ($nL_w(859)$) has a quasi-linear relationship when $nL_w(859)$ is less than ~1 mW cm^{-2} μm^{-1} sr^{-1} in the turbid waters of the Yellow Sea and East China Sea. When $nL_w(859)$ is larger than ~1 mW cm^{-2} μm^{-1} sr^1, the relationship becomes nonlinear until $nL_w(645)$ reaches its maxima with no $nL_w(645)$ changes corresponding to the increase of $nL_w(859)$ as waters get extremely turbid. This phenomenon is attributed to the dominance of $b_b(\lambda)$ for extremely turbid waters in a function of $b_b(\lambda)/(a(\lambda) + b_b(\lambda))$—$a(\lambda)$ and $b_b(\lambda)$ are total absorption coefficient and backscattering coefficient, respectively—of which the normalized water-leaving radiance (or normalized water-leaving reflectance) can be expressed as a function [36]. On the other hand, *Wang et al.* (2009) [6] show that water diffuse attenuation coefficient at the wavelength of 490 nm $K_d(490)$ can be estimated using $nL_w(488)$ and $nL_w(645)$ (or $nL_w(667)$) in the turbid waters. In addition, *Shi and Wang* (2010) [33] show that the NIR normalized water-leaving radiance $nL_w(748)$, $nL_w(859)$, and $nL_w(869)$ from MODIS-Aqua are highly correlated to ocean turbidity, which can be quantified and characterized with $K_d(490)$ in the western Pacific's highly turbid waters, such as those of the Yellow Sea and East China Sea.
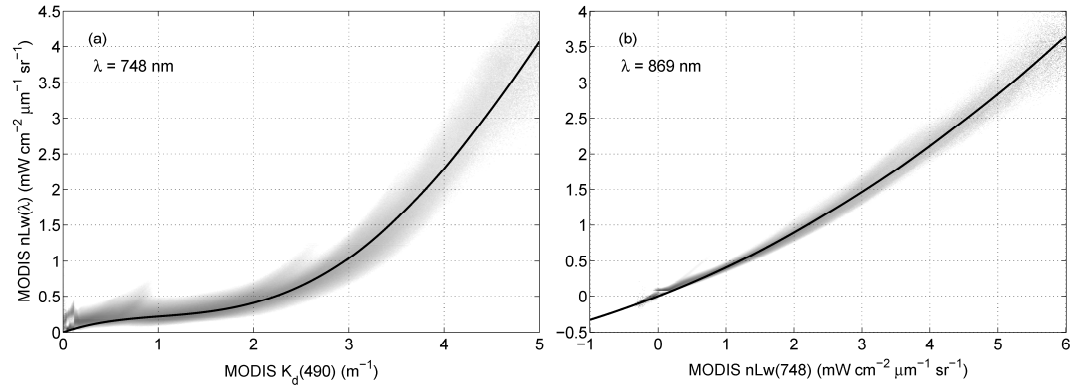
Fig. 2. Scatter plots and empirical polynomial fitting functions for (a) $nL_w(748)$ vs. $K_d(490)$ and (b) $nL_w(869)$ vs. $nL_w(748)$. Note that $nL_w(748)$, $nL_w(869)$, and $K_d(490)$ were derived from MODIS-Aqua measurements (2002 to 2009) using the SWIR atmospheric correction algorithm in this region.

Using the normalized water-leaving radiance at the NIR wavelengths $nL_w(748)$ and $nL_w(869)$, and the corresponding $K_d(490)$ derived using the SWIR atmospheric correction algorithm from MODIS-Aqua measurements in the turbid waters of the western Pacific between 2002 and 2009, the statistical relationships between $nL_w(748)$ and $nL_w(869)$ vs. $K_d(490)$ were derived. Figure 2(a) shows the scatter plots of $nL_w(748)$ vs. $K_d(490)$, as well as an optimal polynomial fitting function between these two parameters. In fact, the empirical polynomial between $nL_w(748)$ and $K_d(490)$ can be expressed as:

$$nL_w(748) = c_1 K_d(490) + c_2 K_d(490)^2 + c_3 K_d(490)^3 + c_4 K_d(490)^4, \qquad (1)$$

where $c_1 = 0.465$, $c_2 = -0.385$, $c_3 = 0.152$, and $c_4 = -0.0121$. Similarly, $nL_w(869)$ (Fig. 2(b)) can be formulated with the following expression:

$$nL_w(869) = b_1 nL_w(748) + b_2 nL_w(748)^2, \qquad (2)$$

where $b_1 = 0.368$ and $b_2 = 0.040$. Obviously, $nL_w(869)$ is also effectively related to $K_d(490)$ through Eq. (1). As shown in Figs. 2(a) and 2(b), the fitting curves match the maximal occurrences of the $nL_w(748)$ (or $nL_w(869)$) and $K_d(490)$ pairs. This is particularly true when $K_d(490)$ is less than ~2 m^{-1}. In the curve fitting, however, it is required that both curves pass through 0 point, i.e., there are no constant terms (no intercepts) in Eqs. (1) and (2). In the range with $K_d(490)$ less than ~2 m^{-1}, $nL_w(748)$ (or $nL_w(869)$) and $K_d(490)$ pairs show less scattering (noise). When the $K_d(490)$ value gets larger, $nL_w(748)$ (or $nL_w(869)$) and $K_d(490)$ pairs show more scattering (noise). Statistical analysis shows that the standard deviation (STD) values of $nL_w(748)$ and $nL_w(869)$ between the direct SWIR retrievals and the estimations of $nL_w(748)$ and $nL_w(869)$ computed from $K_d(490)$ with Eqs. (1) and (2) are about 25.7% and 17.4%, respectively, for $K_d(490)$ ranging between 1 and 5 m^{-1}. This further demonstrates that the empirical relationships between $nL_w(748)$ (or $nL_w(869)$) and $K_d(490)$ can be confidently applied to satellite ocean color data processing in order to estimate and remove the NIR $nL_w(\lambda)$ contributions from the sensor-measured TOA radiances. Consequently, the NIR-based atmospheric correction algorithm [1] with the NIR-corrected $nL_w(\lambda)$ values at wavelengths of 748 and 869 nm can be carried out for the western Pacific region. It is also noted that the maximum of $K_d(490)$ for Eqs. (1) and (2) to estimate the NIR $nL_w(\lambda)$ is 5 m^{-1} because $nL_w(869)$ and $nL_w(748)$ become less sensitive to the change of the ocean turbidity ($K_d(490)$) for the extremely turbid waters.

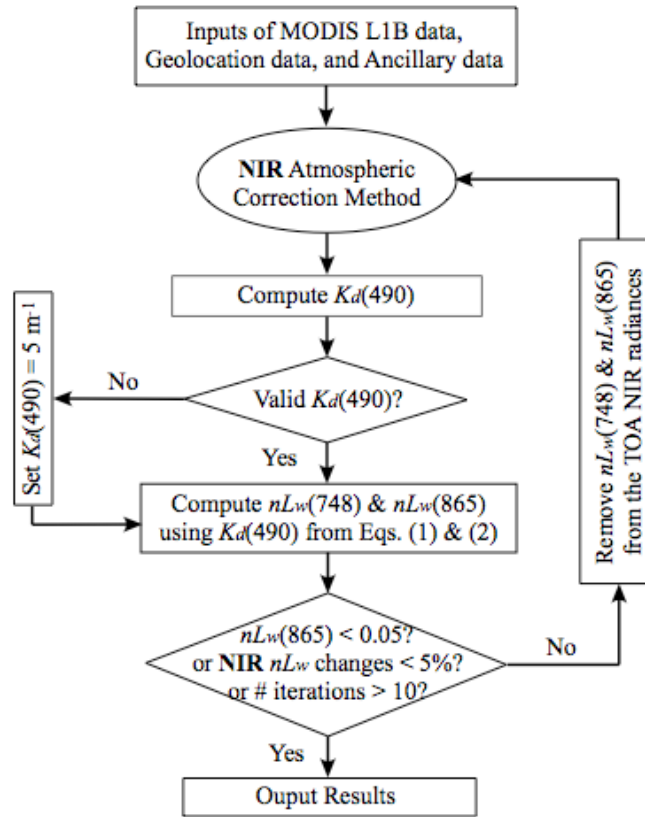## The NIR-Corrected Atmospheric Correction Algorithm for Ocean Color Data Processing

Fig. 3. Schematic flow chart of the new NIR-corrected atmospheric correction algorithm for MODIS-Aqua ocean color data processing in the western Pacific region.

3. Implementation of the NIR-corrected atmospheric correction algorithm

Figure 3 shows the flow chart of the MODIS-Aqua NIR-corrected atmospheric correction and ocean color data processing. An iterative approach is conducted to estimate $nL_w(748)$ and $nL_w(869)$ using Eqs. (1) and (2) with inputs of $K_d(490)$. Three criteria are predefined for the iteration procedure to make sure that $nL_w(748)$ and $nL_w(869)$ are accurately computed and removed in the MODIS-Aqua ocean color data processing:

(1) The derived $nL_w^{(N)}(869) < 0.05$ mW cm^{-2} μm^{-1} sr^{-1} (after second iteration N = 2); or

(2) $nL_w(748)$ and $nL_w(869)$ are converged and stabilized. For the Nth iteration, $nL_w^{(N)}(748)$ and $nL_w^{(N)}(869)$ are outputted as the final estimates only when the difference between the value of $(nL_w^{(N)}(748) + nL_w^{(N)}(869))$ (from Nth iteration) and the value of $[(nL_w^{(N-1)}(748) + nL_w^{(N-1)}(869))]$ (from (N–1)th iteration) is less than 5% (it is changed to 0.5% after this study); or

(3) The number of iterations reaches the maximum of N = 10.

Using stations 1 and 2 as marked in Fig. 1 in the Yellow Sea, the convergence performance of this iterative atmospheric correction scheme has been tested and evaluated for the turbid waters at station 1 (Fig. 4(a)) and highly turbid waters at station 2 (Fig. 4(b)). At station 1, the value of $K_d(490)$ derived from the SWIR atmospheric correction is ~1.9–2.0 m^{-1}. With the iterative NIR atmospheric correction approach, $K_d^{(1)}(490)$ was initially

computed with the assumption of no NIR ocean radiance contributions at 748 and 869 nm for the 1st iteration (N = 1). With the derived $K_d^{(1)}(490)$, $nL_w^{(2)}(748)$ and $nL_w^{(2)}(869)$ are estimated in the
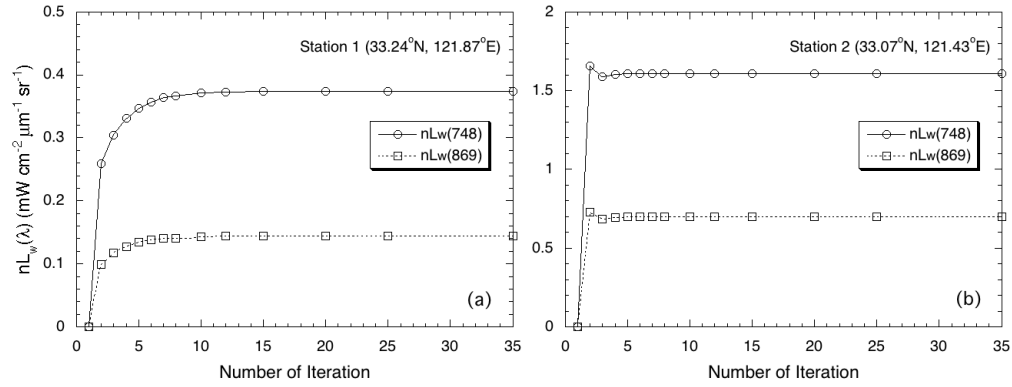

Fig. 4. Changes of $nL_w(748)$ and $nL_w(869)$ estimations as a function of the number of iterations using the NIR-corrected atmospheric correction algorithm for the case of (a) at station 1 and (b) at station 2 for MODIS-Aqua measurements acquired on October 19, 2003. The final $K_d(490)$ values for plots (a) and (b) are 1.96 and 3.49 m^{-1}, respectively.

2nd iteration and $K_d^{(2)}(490)$ is recomputed in order to estimate $nL_w^{(3)}(748)$ and $nL_w^{(3)}(869)$ in the 3rd iteration. At station 1, $nL_w(748)$ and $nL_w(869)$ pairs for the 2nd, 3rd, 4th, and 5th iterations are (0.259, 0.099), (0.304, 0.117), (0.331, 0.127), and (0.347, 0.134) mW cm^{-2} μm^{-1} sr^{-1}, respectively. $nL_w(748)$ and $nL_w(869)$ values eventually converged to (0.374, 0.144) mW cm^{-2} μm^{-1} sr^{-1} at N = 5.

For the highly turbid waters like those at station 2 (Fig. 4(b)), the large NIR ocean radiance contributions can lead to negative $nL_w(\lambda)$ in the visible bands at the 1st iteration, thus with no derived $K_d^{(1)}(490)$. In this case, $K_d(490)$ is setup to be 5 m^{-1} in order to start the iteration process to estimate $nL_w(748)$ and $nL_w(869)$. The estimations of $nL_w(748)$ and $nL_w(869)$ in the following iterations quickly converge as shown in Fig. 4(b) with the final estimations of the $nL_w(748)$ and $nL_w(869)$ pair to be (1.607, 0.698) mW cm^{-2} μm^{-1} sr^{-1}. In general, the criteria of (2) can be met, and $nL_w(748)$ and $nL_w(869)$ can be determined with less than ~5–6 iterations for both turbid waters like those at station 1 and highly turbid waters like those at station 2 in the turbid western Pacific region.

Figure 5 shows $nL_w(\lambda)$ retrievals in the visible and NIR wavelengths, $K_d(490)$, and aerosol optical thickness (AOT) at 869 nm ($\tau_a(869)$) [37] after carrying out the proposed NIR-corrected atmospheric correction approach as described above for the scene acquired by MODIS-Aqua on October 19, 2003. To further evaluate and validate this NIR-corrected atmospheric correction algorithm, the same corresponding ocean color parameters are also produced using the SWIR atmospheric correction algorithm. In general, the normalized water-leaving radiance maps of $nL_w(443)$ (Fig. 5(b)), $nL_w(551)$ (Fig. 5(c)), $nL_w(645)$ (Fig. 5(d)), $nL_w(748)$ (Fig. 5(e)), and $nL_w(869)$ (Fig. 5(f)) derived from this NIR-corrected atmospheric correction are comparable to the corresponding $nL_w(\lambda)$ maps (Figs. 5(i), 5(j), 5(k), 5(l), and 5(m)) derived using the SWIR atmospheric correction algorithm. Some slight differences in $nL_w(\lambda)$ reflect the uncertainty of the atmospheric correction procedure as well as the difference between $nL_w(748)$ (or $nL_w(869)$) estimation from the empirical model and the actual $nL_w(\lambda)$ in the NIR wavelengths as shown in Fig. 2. For the $K_d(490)$ (Figs. 5(a) and 5(h)) with this scene, the values derived from these two atmospheric correction approaches are almost identical. In the AOT $\tau_a(869)$ map derived from the NIR-corrected atmospheric correction approach (Fig. 5(g)), the turbid regions, which show enhanced $nL_w(\lambda)$ in the green (551 nm), red (645 nm), and NIR (748 and 869 nm) wavelengths in the coastal regions of

Yellow Sea and East China Sea, do not have any signatures (Fig. 5(g)). It is consistent with the $\tau_a(869)$ map derived from the SWIR atmospheric correction approach (Fig. 5(n)). This indicates that the ocean radiance contributions in the NIR bands are effectively removed from the MODIS-Aqua TOA radiance measurements using the proposed iterative approach in carrying out the NIR-based atmospheric correction for ocean color data processing.
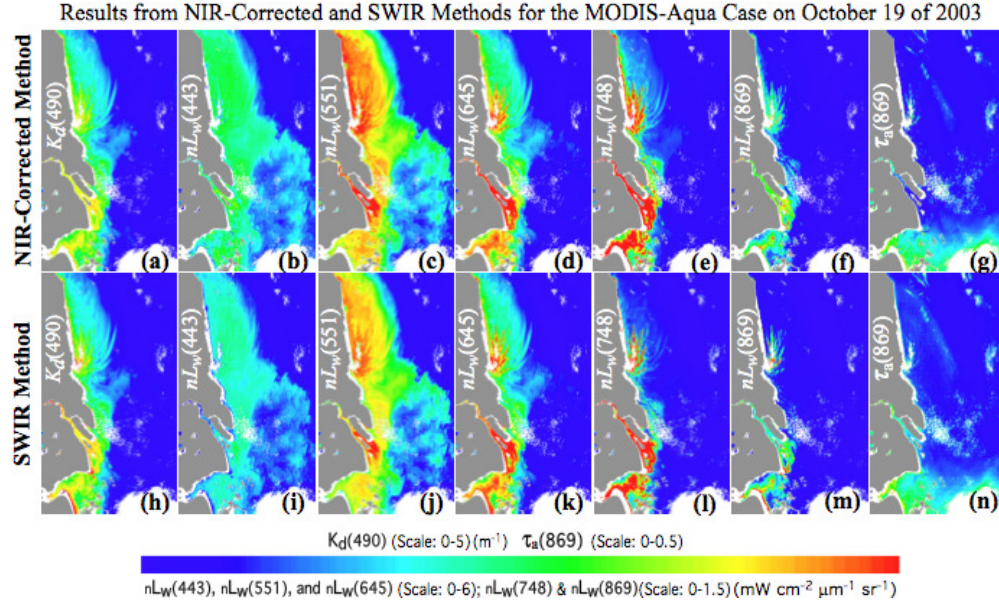

Fig. 5. Comparisons of ocean color retrievals on October 19, 2003 derived from the SWIR atmospheric correction (lower panel) and from the NIR-corrected atmospheric correction (upper panel) for $K_d(490)$ (5(a) and 5(h)), $nL_w(443)$ (5(b) and 5(i)), $nL_w(551)$ (5(c) and 5(j)), $nL_w(645)$ (5(d) and 5(k)), $nL_w(748)$ (5(e) and 5(l)), $nL_w(869)$ (5(f) and 5(m)), and $\tau_a(869)$ (5(g) and 5(n)).

To further evaluate $nL_w(\lambda)$ quantitatively using the NIR-corrected atmospheric correction approach, three sets of $nL_w(\lambda)$ spectra derived from the NIR-corrected, SWIR, and standard-NIR (i.e., no NIR $nL_w(\lambda)$ correction) atmospheric correction algorithms in the turbid waters at station 1 and in highly turbid waters at station 2 are compared and shown in Fig. 6. At station 1, $nL_w(\lambda)$ spectra from the NIR-corrected and the SWIR atmospheric correction approaches are similar with some small differences in the blue and green bands. This is consistent with the $nL_w(\lambda)$ maps derived from these two atmospheric correction algorithms as shown in Fig. 5. Specifically, $nL_w(748)$ and $nL_w(869)$ values derived from these two approaches match very well. In comparison, significant errors of $nL_w(\lambda)$ can be found if the NIR $nL_w(\lambda)$ contributions are not removed when the standard-NIR atmospheric correction was carried out. $nL_w(412)$ values are less than ~0.5 mW cm^{-2} μm^{-1} sr^{-1} from the standard-NIR atmospheric correction approach, while values of $nL_w(412)$ are all over ~2.0 mW cm^{-2} μm^{-1} sr^{-1} from the SWIR and the new NIR-corrected atmospheric correction methods.

Similar to station 1, $nL_w(\lambda)$ spectra derived from the new NIR-corrected and SWIR atmospheric correction approaches are almost identical from the blue to NIR wavelengths at station 2. It is noted that the NIR ocean radiance contributions are very significantly higher at this station than those at station 1. Specifically, $nL_w(748)$ and $nL_w(869)$ values for station 1 (Fig. 6(a)) are 0.36 and 0.15 mW cm^{-2} μm^{-1} sr^{-1}, respectively, compared with those of 1.60 and 0.69 mW cm^{-2} μm^{-1} sr^{-1} at station 2 (Fig. 6(b)). This further demonstrates that the NIR-corrected atmospheric correction approach can be applied to both turbid waters and highly turbid waters. On the other hand, Fig. 6(b) shows that erroneous $nL_w(\lambda)$ can be resulted if the NIR ocean radiance contributions are not accounted for in the atmospheric correction process. At the wavelength of 412 nm, $nL_w(412)$ is less than –3 mW cm^{-2} μm^{-1} sr^{-1} from the standard-

NIR atmospheric correction approach at station 2. In fact, actual values of $nL_w(412)$ derived from the SWIR and the new NIR-corrected atmospheric correction algorithms are ~1.5 mW cm^{-2} μm^{-1} sr^{-1}.
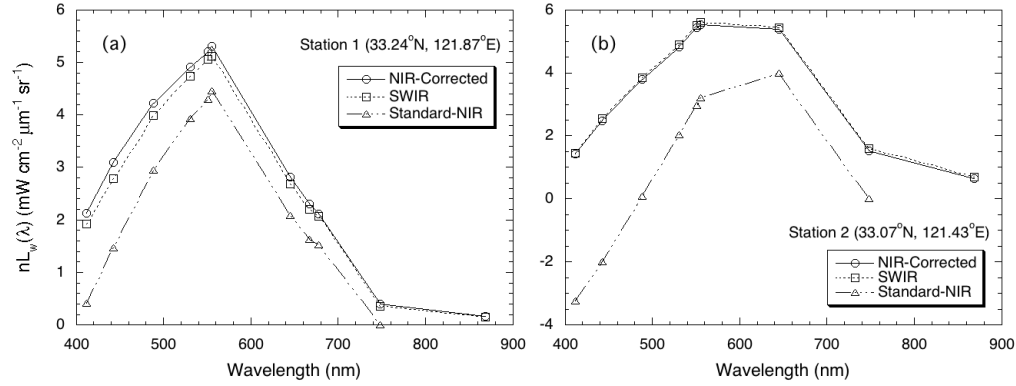

Fig. 6. $nL_w(\lambda)$ spectra derived from the new NIR-corrected atmospheric correction and the SWIR atmospheric correction algorithm for case of (a) at station 1 and (b) at station 2 for MODIS-Aqua measurements acquired on October 19, 2003. For comparison, $nL_w(\lambda)$ spectra derived from standard-NIR atmospheric correction algorithm are also shown in plots (a) and (b).

4. Evaluation of the NIR-corrected atmospheric correction in the western Pacific region

With a scene MODIS-Aqua acquired on October 19, 2003, we show that the new NIR-corrected atmospheric correction algorithm can be applied to western Pacific turbid ocean regions to derive reasonably accurate $nL_w(\lambda)$ spectra that are consistent with those from the SWIR atmospheric correction algorithm. Using the MODIS-Aqua measurements between 2002 and 2010 at stations 1 and 2, the long-term performance of the NIR-corrected atmospheric correction approach has been further evaluated (Fig. 7). Figure 7(a) shows that $nL_w(748)$ and $nL_w(869)$ derived from the SWIR atmospheric correction (indicated as $nL_w^{(SWIR)}(\lambda)$) match well with those from the NIR-corrected atmospheric correction method (indicated as $nL_w^{(NIR-Corr)}(\lambda)$) at station 1. The mean values of $nL_w^{(NIR-Corr)}(748)/nL_w^{(SWIR)}(748)$ and the $nL_w^{(NIR-Corr)}(869)/nL_w^{(SWIR)}(869)$ are 1.02 and 1.00, respectively, with STD values of 0.26 and 0.32. At station 2, Fig. 7(b) shows that $nL_w^{(NIR-Corr)}(748)$ and $nL_w^{(NIR-Corr)}(869)$ are consistent with $nL_w^{(SWIR)}(748)$ and $nL_w^{(SWIR)}(869)$. A slight low bias for both $nL_w^{(NIR-Corr)}(748)$ and $nL_w^{(NIR-Corr)}(869)$ in the high NIR $nL_w(\lambda)$ range reflects the fact that $K_d(490)$ becomes nonlinear and less-sensitive to the increase of $nL_w(\lambda)$ in the NIR wavelengths in the highly turbid water [33]. It is also noted that the number of matchups at station 2 is significantly less than that at station 1. At station 2, MODIS-Aqua sensor for the NIR bands at 748 and 869 nm are more often saturated due to higher ocean turbidity and large $nL_w(\lambda)$ in these two NIR bands.

Figures 7(c) and 7(d) further characterize the performance of the NIR-corrected atmospheric correction algorithm with $nL_w(\lambda)$ retrievals in the MODIS visible bands at stations 1 and 2. At station 1, the mean ratio of $nL_w^{(NIR-Corr)}(\lambda)/nL_w^{(SWIR)}(\lambda)$ for wavelengths of 412, 443, 488, 531, 551, and 645 nm are 1.00, 1.02, 1.01, 1.00, 0.99, and 1.00, respectively. For station 2, $nL_w^{(NIR-Corr)}(\lambda)$ values also appear to be consistent with the corresponding $nL_w^{(SWIR)}(\lambda)$ values. Unlike the slight bias of $nL_w^{(NIR-Corr)}(748)$ and $nL_w^{(NIR-Corr)}(869)$ in the highly turbid waters, no obvious bias of $nL_w^{(NIR-Corr)}(\lambda)$ in the visible bands can be identified. In fact, for station 2 (Fig. 7(d)), the $nL_w(\lambda)$ ratios for bands 412, 443, 488, 531, 551, and 645 nm are 1.03, 1.02, 1.01, 1.03, 0.99, and 1.05, respectively. The consistence of $nL_w^{(NIR-Corr)}(\lambda)$ and $nL_w^{(SWIR)}(\lambda)$ spectra at these two stations suggests that ocean optical, biological, and

biogeochemical properties in the highly turbid western Pacific region can also be computed consistently. However, there are obvious noise errors in the derived products.
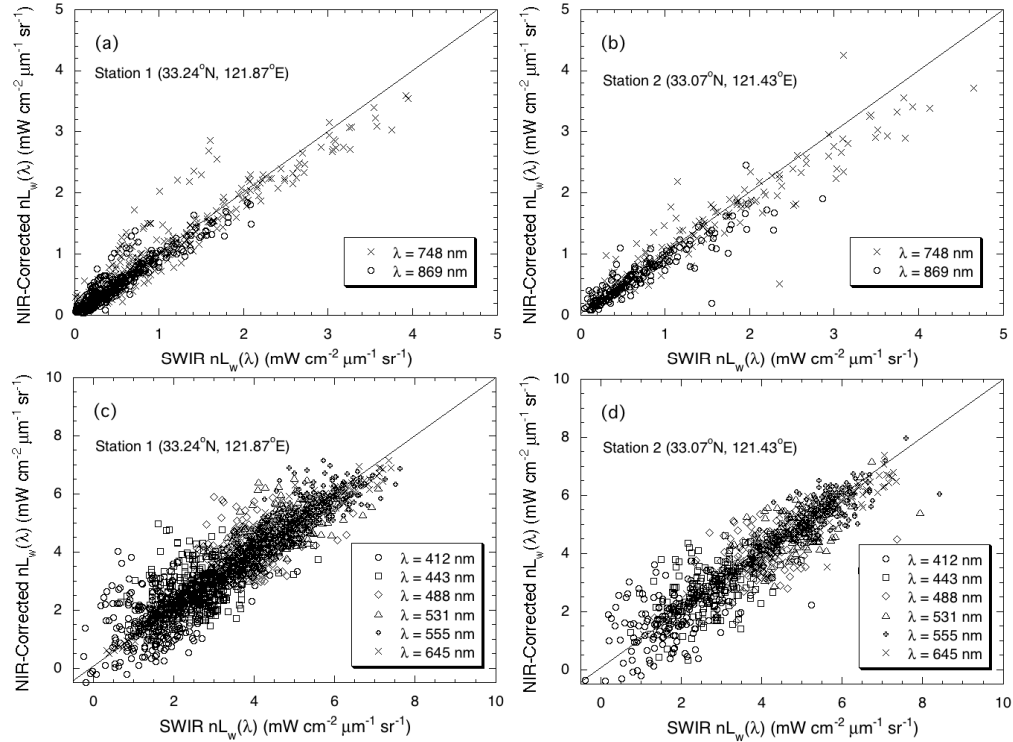

Fig. 7. Matchups of the MODIS-Aqua-measured $nL_w(\lambda)$ spectra (from 2002 to 2010) derived from the new NIR-corrected and SWIR atmospheric correction algorithms for (a) $nL_w(748)$ and $nL_w(869)$ at station 1, (b) $nL_w(748)$ and $nL_w(869)$ at station 2, (c) all $nL_w(\lambda)$ in the visible and NIR bands at station 1, and (d) all $nL_w(\lambda)$ in the visible and NIR bands at station 2.

Figure 8 shows the comparisons of $nL_w^{(NIR\text{-}Corr)}(\lambda)$ and $nL_w^{(SWIR)}(\lambda)$ composite images for wavelengths of 443, 488, 551, 645, 748, and 869 nm from MODIS-Aqua measurements in 2010. Indeed, the $nL_w^{(NIR\text{-}Corr)}(\lambda)$ composite images for each wavelength shows notable similarity to the corresponding $nL_w^{(SWIR)}(\lambda)$ images in terms of both spatial patterns and their magnitudes. In the turbid regions of the Yellow Sea and East China Sea, enhanced $nL_w(\lambda)$ spectra from the blue to NIR wavelengths are observed. The seasonal sediment plume [34] in the central East China Sea can be identified clearly with $nL_w(488)$ (Figs. 8(b) and 8(h)) and $nL_w(551)$ (Figs. 8(c) and 8(i)). In the Hangzhou Bay, Yangtze River estuary, and coastal region of the Yellow Sea, significant elevations of $nL_w(551)$, $nL_w(645)$, $nL_w(748)$, and $nL_w(869)$ were derived from both the new NIR-corrected atmospheric correction algorithm (Figs. 8(c)-8(f)) and the SWIR algorithm (Figs. 8(i)-8(l)). The $nL_w(551)$, $nL_w(645)$, $nL_w(748)$, and $nL_w(869)$ images from these two atmospheric correction approaches are visually identical. It is also worth noting that $nL_w(748)$ and $nL_w(869)$ reach over ~2 and ~1 mW cm^{-2} μm^{-1} sr^{-1} in the Yangtze River Estuary and coastal regions of Yellow Sea. This provides further evidences that the new NIR-corrected atmospheric correction approach cannot only be carried out in moderately turbid regions such as in the central East China Sea plume, but also be applied in the highly turbid coastal zones of the Yangtze River estuary to derive the ocean properties with reasonable accuracy.

5. Discussions and summary

In this study, we developed an iterative approach to carry out a new NIR-corrected atmospheric correction in order to derive MODIS-Aqua ocean color products in the turbid coastal regions of the western Pacific. This approach is for ocean color sensors that do not have the SWIR bands. The NIR $nL_w(\lambda)$ contributions at wavelengths of 748 and 869 nm are estimated from empirical relationships between $nL_w(748)$ (or $nL_w(869)$) and $K_d(490)$, which were derived from the MODIS-Aqua long-term (2002–2009) ocean color retrievals using the SWIR atmospheric correction algorithm. Comparisons between ocean color products with the NIR-corrected atmospheric correction approach and those from the SWIR atmospheric correction algorithm show that the derived $nL_w(\lambda)$ spectra from this new NIR-corrected atmospheric correction algorithm in the western Pacific region match well with the corresponding $nL_w(\lambda)$ from the SWIR atmospheric correction algorithm. *Shi and Wang* (2009) [32] demonstrated that the ocean, in general, is still black for the SWIR bands in China's east coastal regions. *Wang et al.* (2007; 2011) [29, 30] also show that improved and reasonably accurate $nL_w(\lambda)$ spectral data can be achieved with the SWIR-based atmospheric correction in the coastal regions of the Yellow Sea and East China Sea [29], as well as in the highly turbid Lake Taihu [30, 38]. The ocean color products derived from the NIR-SWIR combined atmospheric correction approach have been used to study the ecosystems of the turbid waters, such as the sea surface signature of a sand ridge in the Bohai Sea [39], ocean responses to the Korean dump site of the Yellow Sea [40], the environmental response to a land reclamation project in Korea [41], and the spring-neap tidal effects in this region [42]. The consistence of the ocean color products derived from these two atmospheric correction approaches suggests that the ocean color products from the proposed NIR-corrected atmospheric correction algorithm in the western Pacific region can be used to provide quantitative evaluations of the optical features in the turbid zones.
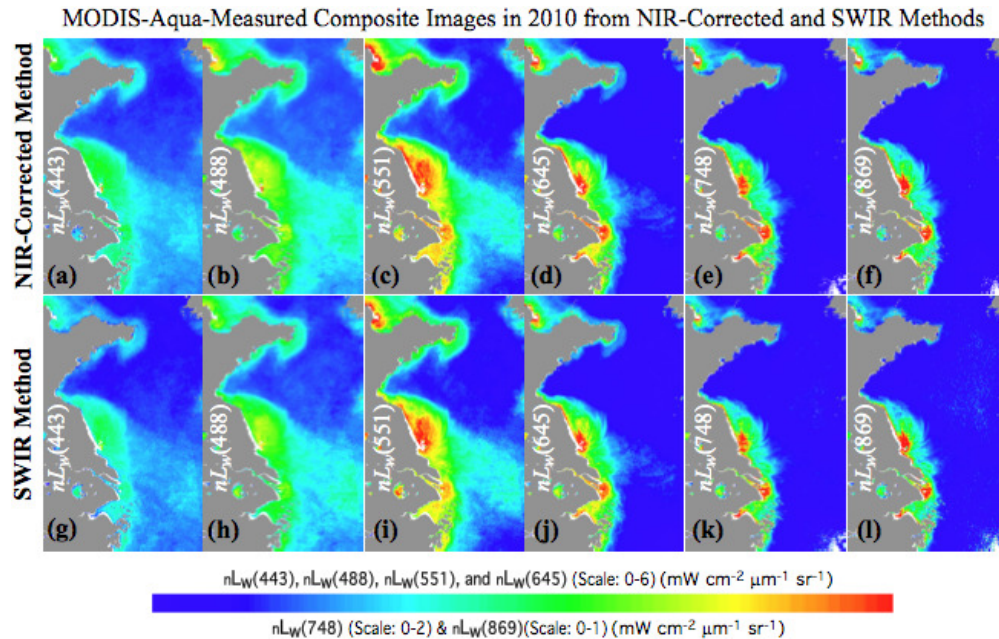

Fig. 8. Comparison of composites of MODIS-Aqua ocean color retrievals in 2010 derived from the new NIR-corrected and the SWIR atmospheric correction algorithms for $nL_w(443)$ (8(a) and 8(g)), $nL_w(488)$ (8(b) and 8(h)), $nL_w(551)$ (8(c) and 8(i)), $nL_w(645)$ (8(d) and 8(j)), $nL_w(748)$ (8(e) and 8(k)), and $nL_w(869)$ (8(f) and 8(l)).

In the proposed NIR-corrected atmospheric correction approach, $K_d(490)$ plays a key role in the process to iteratively compute the $nL_w(748)$ and $nL_w(869)$ values. Since $K_d(490)$ for the

turbid waters is based on semi-analytical optical modeling [6], the NIR-corrected atmospheric correction approach thus implicitly related to the ocean's inherent optical property (IOP) [16]. Even though the relationship between $nL_w(645)$ and $nL_w(748)$ (or $nL_w(869)$) can also be derived from the SWIR-measured $nL_w(\lambda)$ data and applied to estimate $nL_w(748)$ (or $nL_w(869)$), extensive tests (not shown here) show that using the $nL_w(748)$-$K_d(490)$ (or $nL_w(869)$-$K_d(490)$) relationship can make the $nL_w(748)$ (or $nL_w(869)$) estimation less sensitive to the noise of $nL_w(\lambda)$ values. It should be further emphasized that the NIR-corrected atmospheric correction algorithm is based on a regional $nL_w(748)$-$K_d(490)$ (or $nL_w(869)$-$K_d(490)$) model for the Bohai Sea, Yellow Sea, and East China Sea.

There are some limitations for this $K_d(490)$-based, NIR-corrected atmospheric correction approach. First, relationships between $nL_w(748)$ (or $nL_w(869)$) and $K_d(490)$ are developed from long-term MODIS-Aqua observations. Since $nL_w(748)$ (or $nL_w(869)$) and $K_d(490)$ are both dependent on the IOPs in the water, the IOP variability caused by the sediment, phytoplankton, and colored dissolved organic matter (CDOM) can make the $nL_w(748)$-$K_d(490)$ (or the $nL_w(869)$-$K_d(490)$) relationship not exactly the same in the short term as in the long term. On the other hand, the regional dependence of IOPs also indicates that the empirical relationship between $K_d(490)$ and $nL_w(748)$ (or $nL_w(869)$) developed in this study might not be suitable for other highly turbid regions such as the Amazon River estuary and La Plata River estuary, etc. Second, it has been shown [32, 33] that $nL_w(\lambda)$ at the red band (such as $nL_w(645)$) is no longer sensitive to the changes of $nL_w(748)$ (or $nL_w(869)$) in extremely turbid waters. At a certain level, $nL_w(645)$ becomes a constant and does not change with the increase of $nL_w(748)$ (or $nL_w(869)$). This suggests that $K_d(490)$ derived from $nL_w(645)$ for extremely turbid waters ($K_d(490) > \sim 5.0$ m^{-1}) cannot be used to estimate $nL_w(748)$ (or $nL_w(869)$) for the NIR-corrected atmospheric correction algorithm.

Due to the limitations of the $K_d(490)$-based, NIR-corrected atmospheric correction approach, it is necessary to use the SWIR-based algorithm to carry out global ocean color data processing with a uniform atmospheric correction procedure for the turbid regions. On the other hand, the SWIR-based atmospheric correction can also be used to derive accurate ocean color products in extremely turbid waters, where the proposed NIR-corrected atmospheric correction can fail. For the global satellite ocean color observations, some of the sensors such as SeaWiFS and MERIS do not have the SWIR bands. Thus, this study is useful to address the atmospheric correction issues in the highly turbid regions for these sensors. Particularly, GOCI has a local coverage of highly turbid waters in the western Pacific region. Because GOCI has no SWIR bands, atmospheric correction has been a challenge in order to derive reasonably accurate ocean color products in these turbid ocean regions. Methodology and results demonstrated in this study provide an effective alternative for conducting atmospheric correction for GOCI (and other satellite sensors without SWIR bands) ocean color data processing in the turbid regions of the Bohai Sea, Yellow Sea, and East China Sea.

Acknowledgments